scientific reports

Check for updates

OPEN

Research and experiment on a mobile welding robot for expandable convoluted pipe

Shuyan Yao[1,2], Long Xue[2]✉, Jiqiang Huang[2]✉, Bo Chen[2], Ruiying Zhang[2] & Feng Han[2]

Automated welding robots face challenges in unstructured field conditions, limiting their use in complex steel structures like pipelines, bridges, and buildings. Expandable convoluted pipe (ECP) poses unique welding challenges due to their confined spaces and irregular shapes. Manually performed butt-welding for ECPs is inefficient. To address this, a flexible mobile welding robot tailored for ECPs was developed. This paper analyses the robot's structure, working principle, and drive system, minimizing drive chain force-velocity angles to reduce power loss. Transmission modelling, finite element analysis, and life prediction using the Archard model yield promising results. Virtual simulations and prototype welding tests validate the robot's design, with satisfactory weld formation. Expanding the ECP with a hydraulic pump verifies the robot's reliability with no weld cracks observed.

Keywords Expandable convoluted pipe, Mobile welding robot, Flexible contour tracing, Dynamic analysis, Life prediction

Welding is a manufacturing process and technology that joins metals or other thermoplastic materials through heating or high pressure, playing an indispensable role in the development of the manufacturing industry. In 2023, China's steel production amounted to 1.363 billion tons, with more than half of it requiring welding processing, indicating a huge demand for welding. The emergence of industrial welding robots has propelled the welding industry towards high-quality development, playing a pivotal role in enhancing production efficiency, reducing costs, ensuring consistent welding quality, and ultimately boosting enterprise profitability[1–3].

The level of intelligent development in the automotive manufacturing industry has been steadily increasing, resulting in a gradual yearly rise in the proportion of welding robots utilized. In certain advanced automotive manufacturing enterprises, the utilization of welding robots accounts for over 90% of the total welding volume, significantly elevating the standards of intelligent manufacturing within the automotive sector[4]. However, the percentage of automated welding remains comparatively low for unstructured welding applications across various industries. This is particularly evident in the case of construction objects that require on-site welding in complex environments, such as spherical tanks, pipelines, bridges, ships, and architectural steel structures[5,6]. Conventional welding robots struggle to adapt to these challenging scenarios, and welding is mostly performed manually, resulting in low welding efficiency and poor uniformity, which hinders the process of intelligent development in the manufacturing industry.

In order to fulfill the need for automated welding of numerous intricate steel structures on-site, address the confined space challenge posed by industrial welding robots, and broaden their application horizons, scholars globally have conducted extensive research into mobile welding robot technology, and various forms of mobile welding robots have been manufactured[7–23]. Wang et al.[7] developed a no-track adaptive magnetic wheels mobile welding robot specifically designed for fieldwork on spherical tanks and pipelines. This robot is capable of tracing and executing automated welding on three-dimensional curved welds found on spherical tanks, demonstrating its versatility and precision. On the other hand, to address the complexities of manufacturing rigid tracks suitable for unstructured pipeline automation welding and broaden the application realm of rail-based mobile welding robots, Liang et al.[8] pioneered the development of a flexible track mobile welding robot utilizing magnetic seat fixed adsorption. This innovation significantly enhances the flexibility and adaptability of mobile welding robots, opening up new avenues for automation in welding processes. In the realm of on-site construction of architectural steel structures, Guo et al.[9] developed an innovative on-site, all-position rail-mounted welding robot aimed at enhancing the automation and intelligence of welding processes for square box beams. Utilizing a magnetic fixing mechanism, this robot securely attaches a square track to the exterior of the box beam. Subsequently, a welding

[1]China Academy of Machinery Science and Technology Group, Beijing 100044, China. [2]Optoelectronic Equipment Technology Beijing City, Beijing Institute of Petrochemical Technology, Beijing 102617, China. ✉email: xuelong@bipt.edu.cn; huangjiqiang@bipt.edu.cn

carriage traverses along the track, executing all-position welding on the box beam's butt welds. In shipbuilding, Gonzalez-de-Santos et al.[10,11] pioneered the ROWER, a leg-based mobile welding robot that securely attaches to internal partitions within a ship's hull, utilizing a pole-type adsorption device. The alternating forward motion of the adsorption poles facilitates the seamless movement of the entire robot body. Lee et al.[12–17] invented a rail-mounted gantry mobile welding robot specifically designed for double-hull ships, enabling autonomous translation and welding across ship compartment grids. Kermorgant[18] developed a magnetic suction crawler-type mobile welding robot capable of automatically welding regular planar seams on the hull surface. Goh et al.[19,20] introduced a mobile welding robot featuring a three-segment crawler articulated structure, with a welding manipulator positioned on the middle platform. This innovative robot seamlessly moves through unstructured hull compartments to perform automated welding tasks. In order to complete the on-site automatic welding task of large steel structure, Dharmawan et al.[21] devised a mobile welding robot that leverages scaffolding as its track for moving. This robot expertly performs automated welding of intersecting seams on large pipelines, utilizing a manipulator to precisely position the welding torch. Meanwhile, O'Toole et al.[22,23] created a magnetic suction crawler-type wall-climbing welding robot, capable of performing automated welding at any position on the surface of large steel components. These mobile welding robots are capable of performing automated welding on specific, unstructured, and complex curved welds. However, in scenarios involving complex steel structures with limited spaces, conventional mobile welding robots are unable to access these areas, while ordinary welding torches fail to meet the required welding pose. Consequently, manual welding often becomes the sole option, resulting in decreased welding efficiency, inconsistent weld quality, and unreliability. This significantly hinders the need for intelligent technologies development in the manufacturing industry.

The successful application of ECPs in oil exploration represents a technological breakthrough with epoch-making significance[24,25]. However, these pipes have a complex structure with narrow space and special-shaped cross-section. At present, most of them are welded by manual welding, which has low welding efficiency and poor welding uniformity. To address this industry-wide challenge, a flexible contour tracing mobile welding robot is proposed in this paper, specifically engineered for welding complex curved surfaces in confined spaces. The dynamic analysis of the drive system is carried out, and the life prediction of the robot is conducted. Additionally, an engineering prototype has been fabricated specifically for welding tests. The experimental results confirmed that the mobile welding robot can successfully complete welding tasks on ECPs, achieving excellent weld quality. Notably, the welds remain intact during pipe expansion, demonstrating the robot's engineering practicality. This innovation effectively addresses the persistent challenges that have long plagued the oil well cementing and maintenance industry. This groundbreaking innovation effectively addresses the persistent challenges that have long plagued the oil well cementing and maintenance industry.

Structure design of the robot

In the field of oil exploration and drilling, complex geological conditions and technological limitations often lead to complex scenarios such as wellbore leakage and wellbore collapse[26–28]. To ensure the smooth progress of subsequent drilling operations, the application of ECP technology for wellbore reinforcement and repair has emerged as an ideal solution to solve these problems. The specific workflow involves butt welding of fixed-length ECPs to form a pipe string, which is then inserted into the wellbore requiring repair. Once the pipe string reaches the designated repair location, it is expanded to restore its circular shape through hydraulic or mechanical expansion methods, effectively sealing off leaks and repairing complex subterranean formations. The complex structure of ECP necessitates a significant reliance on manual welding, thus making it imperative to urgently develop a specialized welding robot that can boost welding efficiency and guarantee consistent weld seams.

Introduction to the 8-shaped ECP

The ECP is a metal pipe made by pressing and rolling a metal material with a large plastic deformation. It can be classified into single-sided concave, double-sided concave, and multi-sided concave shapes based on its different appearance[29]. The double-sided concave shape, commonly known as the 8-shaped, is widely used in cementing and repair operations in industrial settings due to its ease of extrusion molding and balanced structural complexity. There are narrow spaces at the concave ends of the ECP, with a minimum curvature radius of 25 mm, and its structure is shown in Fig. 1. During the maintenance of oil wellheads, it is necessary to butt-weld fixed-specification ECPs into pipe string at the wellhead and put it into the underground. However, welding operations often occur outdoors, making it difficult to apply traditional industrial welding robots. Currently, the butt-welding of ECPs is mainly carried out manually, which results in low welding efficiency and poor uniformity, significantly hindering the intelligent development of the oil well cementing and repair industry.

Robot structure analysis and design

The 8-shaped ECP, with its narrow spaces and complex cross-sectional shape, poses a challenge for conventional mobile welding robots to access the concave areas at both ends. Additionally, ordinary welding torches cannot carry out welding operations in the optimal welding posture due to size constraints. To tackle this, a design concept is proposed that involves a micro-vehicle equipped with a miniature specialized welding torch for robotic structure design. However, actuating the micro welding vehicle brings a fresh set of challenges. To address this, we drew inspiration from the mechanical structure of soft robots[30,31], connecting multiple micro-vehicles in series and adopting a chain drive design concept to include a power source. A rigid contour tracing track guides the vehicle system in the mechanical track, ensuring that each micro-vehicle follows a fixed path. By affixing the specialized miniature welding torch to any micro-vehicle, the entire weld seam around the pipe can be completed in a single revolution. Furthermore, employing double-row flexible drive chains instead of micro-mobile vehicles significantly reduces the robot's manufacturing cost, thereby enhancing the engineering application of flexible mobile welding robots for ECPs.

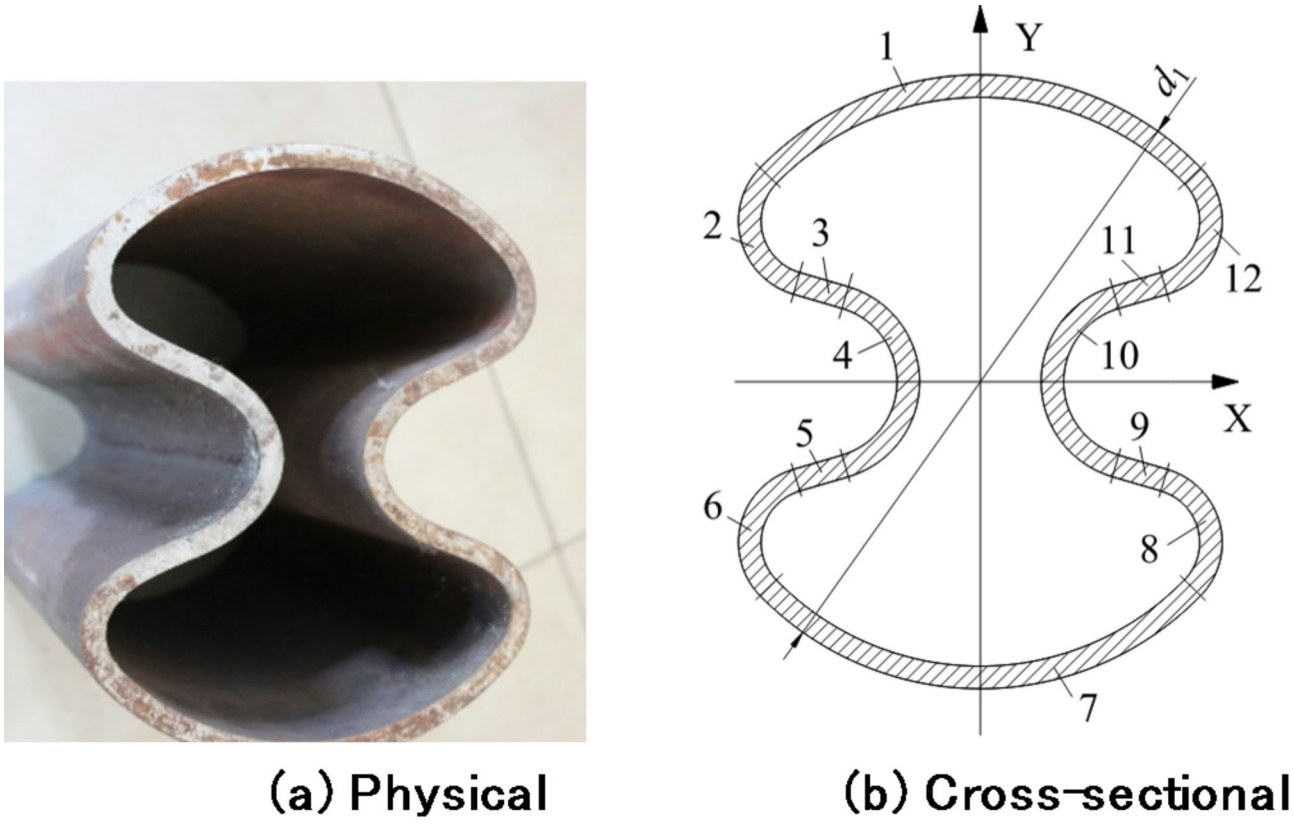

Fig. 1. The structure of 8-shaped ECP.

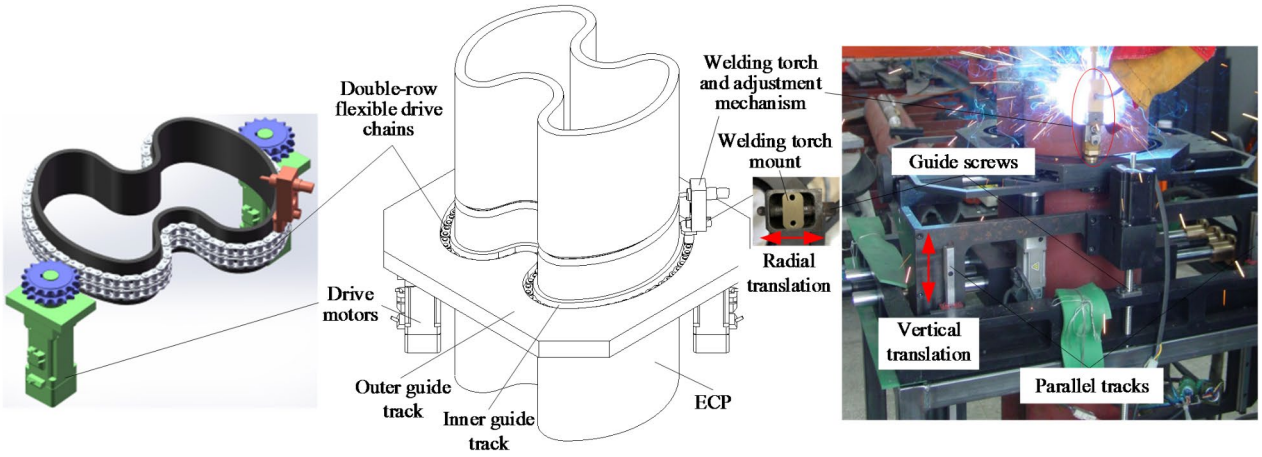

Fig. 2. Structure of mobile welding robot for 8-shaped ECP.

The structural schematic of the flexible mobile welding robot for the 8-shaped ECP is shown in Fig. 2. This welding robot primarily consists of an inner guide track, an outer guide track, double-row flexible drive chains, drive motors, a welding torch adjustment mechanism, and a welding torch. The welding torch adjustment mechanism securely holds the miniature welding torch in alignment with the weld seam groove and is fixedly mounted on the drive chain through mechanical structures. The combination of the inner and outer guide tracks serves to constrain the position of the drive chains. Two high-power stepper motors are installed on the outer guide track, and they are actuated to move synchronously through a control system, propelling the drive chains along the guide tracks. By welding along the seam of the ECP with the tip of the miniature welding torch for one revolution, a continuous weld can be formed. This process is repeated several times to accomplish the butt welding of the ECP.

The flexible contour tracing mobile welding robot introduces a novel configuration, revolutionizing the capabilities of mobile welding robots. Its drive system employs a flexible contour tracing structure design that incorporates an inner guide track, drive chain mechanism, and outer guide track. This design mirrors the contour of the weld seam of the workpiece to be welded, with the overall track divided into an inner track and an outer track. The split-type structural design simplifies the processing, manufacturing, and installation of the robot's drive system. To minimize transmission friction and enhance stability in intricate contours, a double-row roller drive chain is selected as the flexible transmission actuator. Grooves are incorporated along the sides of the inner and outer tracks to guide the rolling of the rollers, thus minimizing friction resistance during transmission. This flexible contour tracing mobile robot configuration, combined with the micro welding torch structure, significantly enhances the accessibility of mobile welding robots, making it an ideal choice for welding workpieces featuring complex and narrow weld seam contours. This offers a groundbreaking design approach for flexible welding manufacturing across various industries.

The conventional chain transmission typically comprises a driving sprocket, a driven sprocket, and a chain looped around them[32,33]. In this mechanism, the chain acts as a flexible intermediary, relaying torque from the driving sprocket to the driven sprocket through the engagement of their teeth. This transmission process inherently involves a tensioned side and a looser side of the chain. In contrast to the vertical plane operation of traditional chain transmission, the drive chain employed in the flexible contour tracing mobile welding robot for ECPs performs its drive force transmission on a horizontal plane. This chain link, which carries the welding torch, doubles as a mobile carrier trolley, acting as the actuator responsible for guiding the welding torch along the weld seam to accomplish the butt welding of the pipe. Within the structural design framework of the robot outlined in this paper, the drive chain moves within a contour tracing track, involving both rolling and sliding friction. The friction force encountered is significantly higher than that encountered in conventional chain transmission, rendering the standard calculation formulas inapplicable. Consequently, a novel drive force transmission model is necessary to analyze and compute the dynamics during the transmission process, providing crucial guidance for the overall structural design.

Dynamic analysis and calculation of drive system

The welding of ECPs can be regarded as a welding operation conducted within the same horizontal plane, where the welding speed during the process can be considered constant. To further gain a deeper understanding of the transmission laws of this novel chain structure and thereby optimize the mechanical design of the robot, it is necessary to conduct dynamic analysis and calculations of its transmission process. Based on these calculations, the structure of the robot can be optimized accordingly.

Dynamic analysis of drive chain

When the drive chain operates at a constant speed, the forces exerted on the chain pin of the drive chain on the convex arc surface of the ECP is illustrated in Fig. 3. The motor provides the driving torque, which is transferred to the chain through the sprocket. Each chain pin of the chain link bears the tensile force from the chain plates between adjacent chain links. The directions of the forward tensile force F_i and the backward tensile force F_{i-1} are along the centerlines of the front and rear chain plates, respectively. The angles formed in the forward and backward directions between the direction of the tensile force and the chain pin velocity vector are defined as α_i and β_i, respectively. The curvature radius of the contour tracing track surface at the contact point between each chain link and the contour tracing track arc is ρ_i, while the arc radius of the contact position between the drive chain link and the contour tracing track is r. The chain pitch is P. After the sprocket is tensioned, the track support force is F_{ni}, and the mixed friction force at each chain pin is mainly the combined sliding friction force F_{fi}. Since the mass of the chain link is relatively small, its gravitational force is neglected. Based on geometric relationships, it can be obtained that

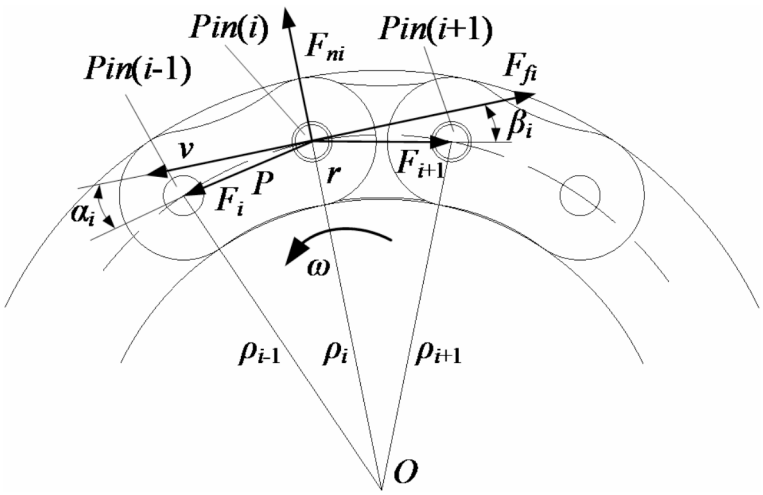

Fig. 3. The force diagram of drive chain pin shaft.

$$\begin{cases} \sin\alpha_i = \dfrac{P^2 + (\rho_i + r)^2 - (\rho_{i-1} + r)^2}{2P(\rho_i + r)} \\ \sin\beta_i = \dfrac{P^2 + (\rho_i + r)^2 - (\rho_{i+1} + r)^2}{2P(\rho_i + r)} \\ 0 \leqslant \alpha_i \leqslant \dfrac{\pi}{2} \\ 0 \leqslant \beta_i \leqslant \dfrac{\pi}{2} \\ i = 1, 2, 3 \ldots\ldots \end{cases} \tag{1}$$

During the welding process, the welding torch is actuated by the drive chain at a constant speed, and the entire drive system remains in a state of force balance. Assuming a comprehensive friction coefficient between the drive chain and the contour tracing track is μ, a force analysis on a single chain pin reveals the following as

$$\begin{cases} F_i \cos\alpha_i = F_{i+1}\cos\beta_i + F_{fi} \\ F_{ni} = F_i \sin\alpha_i + F_{i+1}\sin\beta_i \\ F_{fi} = \mu F_{ni} \end{cases} \tag{2}$$

The inner wall contour of the contour tracing track for the ECP can be regarded as being composed of multiple arcs or straight lines connected tangentially. When the chain pins *i*-1, *i*, and *i*+1 transmit motion along the same arc segment, it can be concluded that

$$\begin{cases} \rho_{i-1} = \rho_i = \rho_{i+1} \\ \alpha_i = \beta_i \end{cases} \tag{3}$$

Equation (2) can be written as

$$F_i \cos\alpha_i = F_{i+1}\cos\beta_i + \mu F_i \sin\alpha_i + \mu F_{i+1}\sin\beta_i \tag{4}$$

It can be obtained that from Eq. (4)

$$F_{i+1} = F_i \frac{\cos\alpha_i - \mu\sin\alpha_i}{\cos\beta_i + \mu\sin\beta_i} \tag{5}$$

Equation (5) represents the driving force transfer equation at each link pin shaft of the flexible contour tracing drive system during uniform movement. Given the initial driving force of the motor, the driving force at the pin shaft of each link can be deduced.

Before welding, the drive system of the flexible contour tracing mobile welding robot remains stationary, with no driving force or frictional force present in the device. Once activated, the driving force gradually increases, causing the chain links to tension accordingly. When the driving force reaches a critical state, where it matches the total frictional resistance within the device, the welding arc is initiated by the welding torch as the device begins to move. At this point, the drive chain propels the welding torch to move at a constant speed along the flexible contour tracing track, and the drive system attains a state of equilibrium. The driving force remains balanced due to the polygonal characteristics of the chain drive.

From Eq. (2), the friction resistance at the position of the *i*-th chain pin is obtained as

$$F_{fi} = \mu F_i \sin\alpha_i + \mu F_{i+1}\sin\beta_i \tag{6}$$

Assuming that the flexible drive chain consists of *n* chain links, as the drive system operates as a closed loop with interconnected ends, the friction resistance of the *n*-th chain link can be derived as follows

$$F_{fn} = \mu F_n \sin\alpha_n + \mu F_{n+1}\sin\beta_n \tag{7}$$

Where F_{n+1} denotes the tensile force applied by the first chain pin onto the *n*-th chain pin. Consequently, the driving force necessary for the device's operation can be expressed as

$$F = \sum_{i=1}^{n} F_{fi} = \sum_{i=1}^{n} (\mu F_i \sin\alpha_i + \mu F_{i+1}\sin\beta_i) \tag{8}$$

Based on Eq. (8) and the actual drive conditions, the total driving force required for the entire flexible drive system can be calculated. Subsequently, an appropriate driving motor and its quantity can be selected accordingly. Generally, the number of driving motors configured should be no less than two, which is more conducive to the long-life and high-efficiency operation of the ECP mobile welding robot.

Laws of driving force transmission

The flexible contour tracing transmission trajectory of the ECP mobile welding robot exhibits a complex shape, with varying friction resistance at arcs with different radii of curvature. The pattern of attenuation experienced

by the motor driving force during transmission primarily depends on the angles α_i and β_i between the front and rear tensile forces acting on the chain pin of the drive chain and the direction of the velocity vector. Based on Eq. (5), a recursive formula for calculating the driving force within the drive chain can be derived, and the driving force transmission coefficient a can be expressed as

$$a = \frac{\cos\alpha_i - \mu\sin\alpha_i}{\cos\beta_i + \mu\sin\beta_i} \tag{9}$$

The driving force transmission coefficient 'a' represents the ratio of the transmission value of the driving force when the front and rear pins of the drive chain pass through a single chain link. Analysis reveals that, under ideal conditions, a higher value of 'a' results in a more optimal transmission process, with less attenuation of driving force during transmission. Consequently, this results in a lower requirement for driving motor power in the robot's transmission system, a simpler hardware configuration, and improved energy efficiency during operation.

According to Eq. (9), the value of the driving force transmission coefficient 'a' depends on the angle between force and velocity, α_i and β_i, as well as the comprehensive friction coefficient μ. In well-lubricated transmission conditions, the sliding friction coefficient for carbon steels ranges approximately from 0.09 to 0.19, while the rolling friction coefficient is approximately 1/60 to 1/40 of the sliding friction coefficient. Based on practical engineering experience, the comprehensive friction coefficient μ can be taken as 0.2. When adjacent drive chain pins are located on the same arc segment of the flexible contour tracing track, the values of α_i and β_i are equal, as derived from Eq. (2). Under such conditions, the relationship between the driving force transmission coefficient 'a' and the angle α_i (β_i) between the velocity vector and the direction of tensile force is depicted in Fig. 4. It can be observed from the figure that, on the same arc segment, the driving force transmission coefficient 'a' exhibits a linear relationship with the angle α_i (β_i). A smaller value of α_i (β_i) corresponds to a higher value of 'a'. When the contour tracing track is a straight line, the radius of curvature approaches infinity, and the driving force transmission coefficient 'a' attains its limiting value of 1, indicating nearly lossless transmission of driving force.

When adjacent chain links are positioned on arcs with different radii of curvature, the relationship between the driving force transmission coefficient 'a' and the force-velocity angles α_i and β_i is illustrated in Fig. 5. Assuming a fixed value for the comprehensive friction coefficient, the transmission coefficient 'a' exhibits a trend of decreasing first and then increasing as the angle α_i increases, while it gradually decreases as the angle β_i increases. Therefore, during the flexible contour tracing transmission process, it is necessary to comprehensively consider the curvature radius values at the junctions of the contour tracing track arcs. By increasing the curvature radii at each contour tracing track section, the force-velocity angles α_i and β_i formed at the chain pins can be minimized, which effectively enhances the value of the driving force transmission coefficient and reduces energy losses during the transmission process.

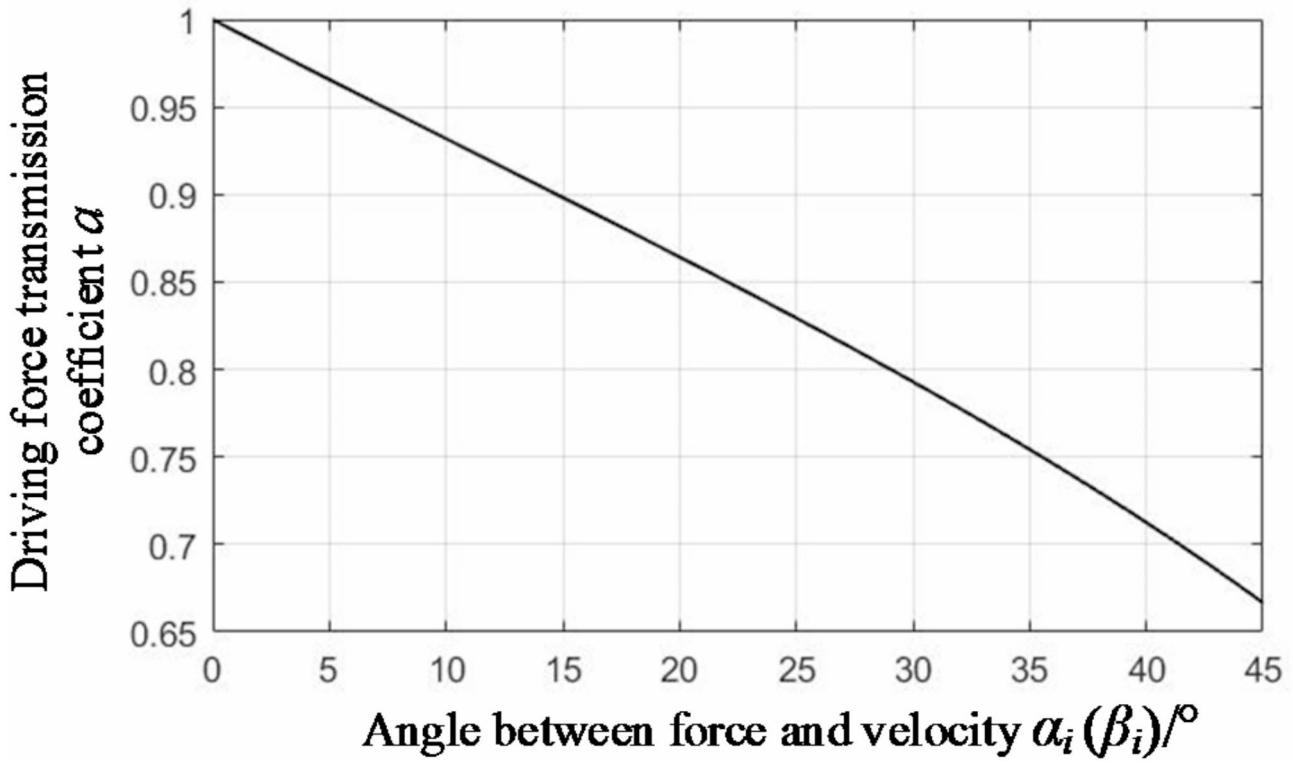

Fig. 4. The driving force transmission coefficient 'a' varies with the angle'α_i' (or 'β_i').

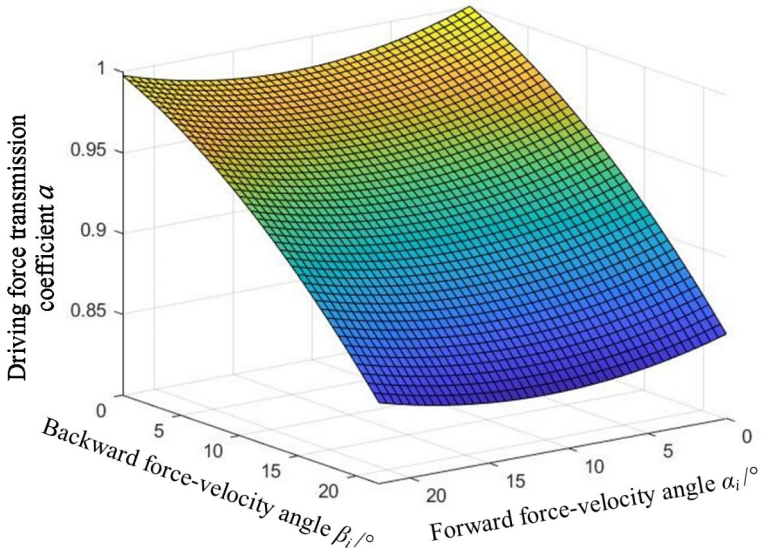

Fig. 5. The driving force transmission coefficient '*a*' varies with the angles 'α_i' and 'β_i'.

Life prediction of the robot

During the robot transmission process, the drive chain carries a miniature welding torch and moves within the contour tracing track. Both rolling friction and sliding friction exist between the drive chain and the contour tracing track. As the robot accumulates working hours, the wear between the contour tracing track and the drive chain gradually increases. To ensure the stable operation of the welding robot system, it is necessary to predict the lifespan of the robot. The drive chain, as a vulnerable standard component, requires regular replacement. The contour tracing track, as an essential part of the robot, is considered to have reached the end of its lifespan when the wear exceeds the thickness of the surface hardening layer. Therefore, the lifespan of the ECP mobile welding robot is predicted based on the working duration when the wear exceeds the thickness of the surface hardening layer.

Transmission model construction and finite element analysis

Based on the actual structural dimensions of the ECP mobile welding robot, a flexible transmission simulation model was established and finite element meshing of stress concentration area was conducted as shown in Fig. 6. According to the theory of material mechanics, at the location where the curvature radius of the contour tracing track is relatively small, the transmission direction of the drive chain changes rapidly, resulting in stress concentration. This area is prone to structural damage[34,35]. Therefore, this paper focuses on the finite element analysis of the recessed area on the outer contour tracing track.

Both the contour tracing track and the drive chain are made of 45 steel with a yield strength of 355 MPa. The maximum driving force provided by the robot's motor is 500 N. A tensile force of 500 N is applied to the drive chain along the tangent direction of the contour tracing track's arc surface. Assuming a rigid connection between the contour tracing track and the drive chain roller, the finite element simulation results are shown in Fig. 7. Figure 7a indicates that the maximum equivalent stress is 15.19 MPa, which is far below the yield strength of the material. Figure 7b reveals that the total deformation is 1.09 μm, and it occurs on the drive chain, with even smaller deformations observed on the contour tracing track. In summary, the structural design strength and stiffness of the ECP flexible contour tracing mobile welding robot both meet the design requirements.

Robot life prediction based on Archard model

The primary failure modes of the ECP flexible contour tracing mobile welding robot can be categorized into strength failure, insufficient stiffness, and wear failure. Based on the finite element analysis results of the flexible drive chain, the drive system demonstrates satisfactory strength and stiffness, adhering to the established requirements. Consequently, wear failure of the flexible contour tracing track is anticipated to be the principal failure mode that significantly impacts the lifespan of the robot.

The drive chain operates within the flexible contour tracing track, and its wear primarily manifests as abrasive wear and adhesive wear, which can be evaluated and calculated using the Archard classical wear theory model[36–38]. During welding with the ECP, the welding speed is set to 5 mm/s, resulting in a relatively low transmission speed and insignificant frictional heating. Therefore, the influence of temperature on the wear process can be neglected in the calculation. The amount of wear is directly proportional to the sliding speed, normal load on the contact surface, and the duration of wear, while it is inversely proportional to the material hardness of the drive chain and contour tracing track. Based on the wear model and extensive experimental results, the wear volume satisfies the following formula

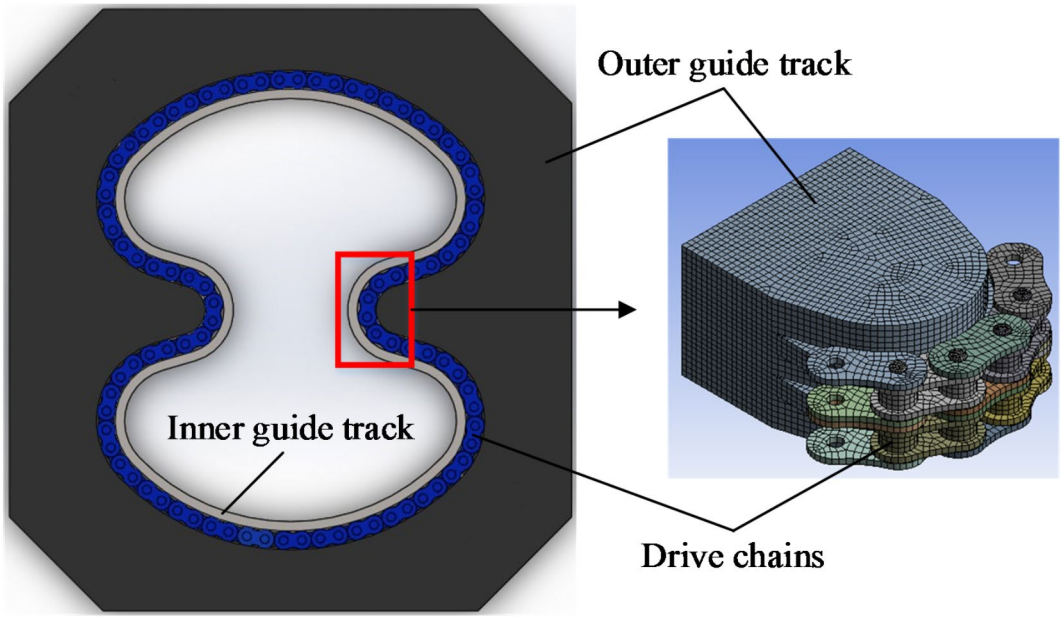

Fig. 6. Transmission model and finite element analysis meshing of stress concentration area.

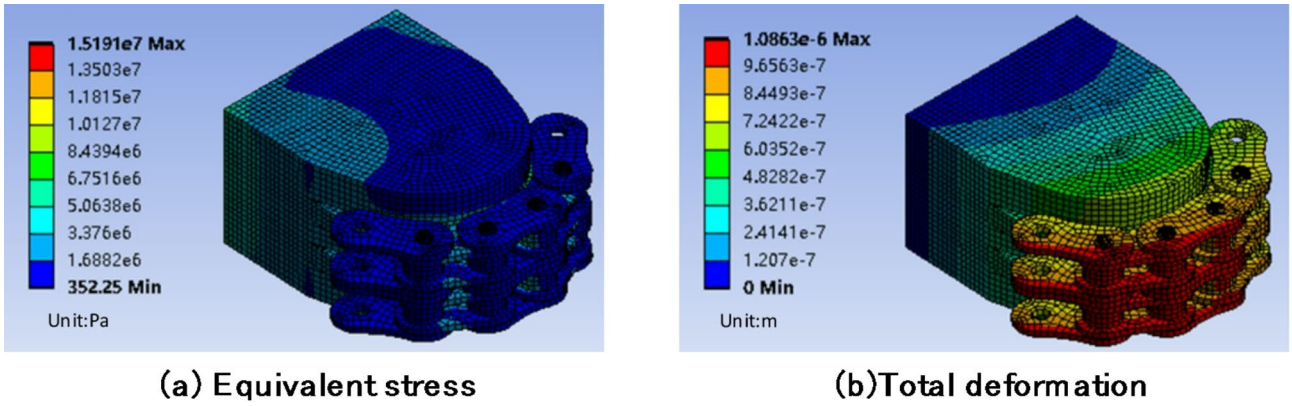

Fig. 7. The finite element analysis results of the stress concentration area.

$$\mathrm{d}V = K\frac{\mathrm{d}P \cdot \mathrm{d}L}{H} \tag{10}$$

In Eq. (10), dV stands for the wear volume of the material, while dL represents the relative sliding distance of the contact surface, The normal load is denoted by dP, and H signifies the hardness of the material. Assuming temperature has a negligible impact, its value can be deemed constant, often approximated as $H = 2.8\ R_{eL}$, where R_{eL} refers to the yield strength of the material. The wear coefficient, designated as K, is influenced by multiple factors, including contact materials, lubrication conditions, and the working environment. Typically, its value is determined experimentally and ranges from 10^{-8} to 10^{-3}. In this paper, the value of K is adopted as 3×10^{-6}.

The expressions for dV, dL, and dP in Eq. (10) can be written as

$$\begin{cases} \mathrm{d}V = \mathrm{d}h \cdot \mathrm{d}A \\ \mathrm{d}P = \sigma \mathrm{d}A \\ \mathrm{d}L = u\mathrm{d}t \end{cases} \tag{11}$$

In Eq. (11), dh signifies the wear depth, dA represents the contact area, σ denotes the normal stress, u indicates the sliding speed, and dt stands for the sliding time. By substituting Eq. (11) into Eq. (10), we arrive at the following result

$$\mathrm{d}h = \frac{K\sigma u}{H}\mathrm{d}t \tag{12}$$

The integral on both sides of the Eq. (12) can be obtained

$$h = \frac{K\sigma u}{H}\int_0^t \mathrm{d}t \tag{13}$$

Assuming that h_1 represents the amount of rail wear when the drive chain is transmitted for one cycle, it can be obtained from Eq. (13)

$$h_1 = \frac{K\sigma u n}{H} \tag{14}$$

In Eq. (14), n represents the number of rollers in the drive chain, which is also the number of transmission chain links. Based on the actual engineering prototype, we have determined that n equals 88. σ is taken as the maximum equivalent stress value of 15.19 MPa, and the sliding speed u is the same as the welding speed. For 45 steel, after surface quenching, the R_{eL} value is designated as 1950 MPa. Using Eq. (14), the rail wear amount h_1 for one revolution of the drive chain is calculated as 3.672×10^{-9}m. The thickness of the hardened surface layer of the contour tracing track is set as $B=2.5$ mm. Once the hardened layer is completely worn out, the robot is considered to have failed due to wear. The lifespan of the robot is expressed in terms of the number of welding cycles.

$$N = \frac{B}{h_1} \tag{15}$$

By substituting the known conditions into Eq. (15), the life of the robot can be calculated. According to the measurement results, the total length of the contour tracing track is 839.84 mm, and it takes 167.97s for the drive chain to complete one revolution. Our calculations indicate that the lifespan of the robotic system is 3.176×10^4 hours. Since many of the parameters used in the calculations are relatively conservative, the actual lifespan of the inflatable bellows mobile welding robot exceeds the calculated value. However, due to variations in the robot's actual operating environment and various other influencing factors, this calculated lifespan should be used as a reference only by professionals in the field.

Trajectory simulation and experimental verification

To guarantee that the flexible contour tracing mobile welding robot is capable of executing butt welding operations on the 8-shaped ECPs, a virtual simulation platform was established, utilizing MATLAB software to carry out trajectory simulations, and a prototype was fabricated for conducting actual welding experiments, in order to corroborate the effectiveness of the robot designed in this study. To assess the practicality of the ECP mobile welding robot, the welded ECP underwent pressurization and expansion to achieve a circular form. Upon thorough inspection, no cracks were detected in the weld following expansion, thus validating the reliability of the robot's automated welding process.

Trajectory simulation

A virtual simulation platform was established in MATLAB software to conduct simulation experiments for verification. Appropriate simulation parameters were set, including a diameter of $d_1=225$ mm for the outermost layer of the ECP, and an offset distance of $e=10$ mm between the projection of the outermost contour line of the ECP and the central contour line of the flexible contour tracing drive chain in the horizontal plane, with a projection distance of 54.5 mm in the vertical direction. The simulation results are shown in Fig. 8, where the red line represents the running trajectory of the flexible contour tracing drive chain, which is the movement path of the welding vehicle, and the blue trajectory represents the movement path of the welding torch end. As the welding vehicle moves along the red trajectory of the ECP for one revolution, the welding torch end moves along the blue trajectory for one revolution as well. The trajectory of the welding torch end aligns with the groove section of the 8-shaped ECP to be welded, indicating accurate welding capability. This demonstrates that the robot designed in this study can accurately achieve the 8-shaped trajectory, thus verifying the feasibility of the flexible contour tracing mobile welding robot.

Experiment

To validate the reliability of the flexible contour tracing mobile welding robot, an engineering prototype was manufactured specifically for welding experiments, and a pressurized expansion test was subsequently conducted on the welded ECP. In particular, an automatic butt-welding test prototype tailored for an 8-shaped ECP was developed, boasting an outermost diameter of 225 mm and a wall thickness of 8 mm. The welding test platform is shown in Fig. 9.

According to the welding process requirements for butt welding of ECP, MIG welding was chosen, employing a solid welding wire of JM-56 with a diameter of 1.0 mm. The shielding gas was composed of a blend of 80% Ar and 20% CO_2. A welding path planning approach consisting of two layers and three passes was adopted, with the welding process parameters outlined in Table 1. Initially, a surfacing welding test was conducted on the ECPs, yielding satisfactory outcomes. Subsequently, welding experiments were carried out on standard butt-welding samples of the ECPs. As depicted in Fig. 10, the welded specimens exhibited excellent weld bead formation and a high level of welding quality.

To further verify the reliability of the ECP mobile welding robot in practical engineering applications, two ECPs with an initial diameter of 241.3 mm were butt welded. After welding, one end of the bellows was welded

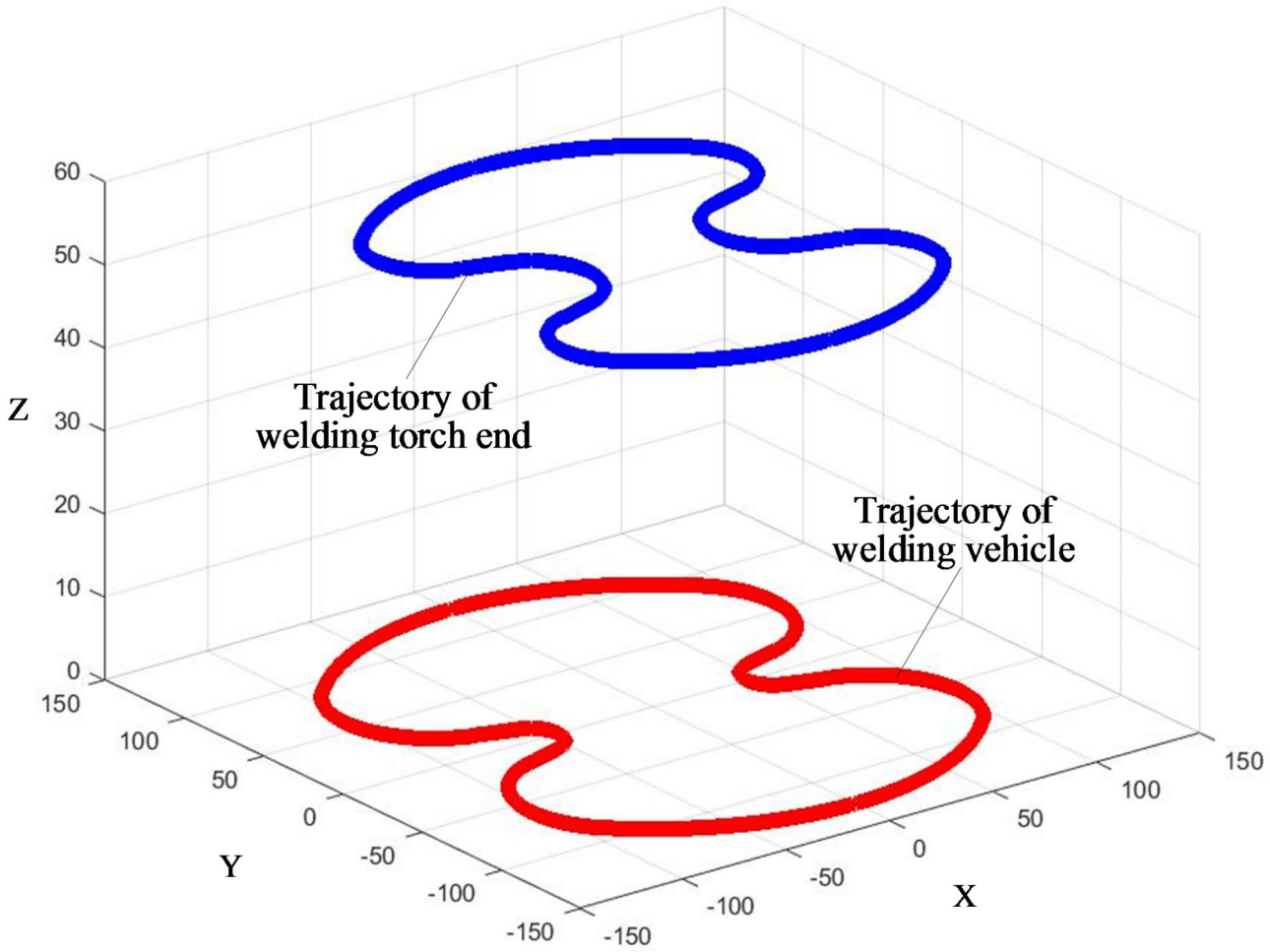

Fig. 8. The trajectory simulation of welding vehicle and welding torch end.

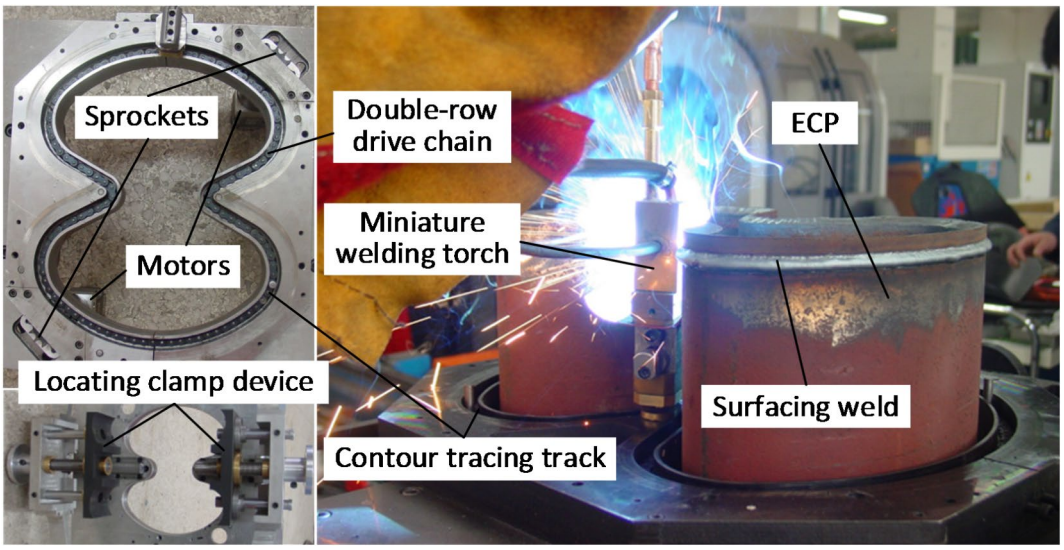

Fig. 9. The welding test platform of 8-shaped ECP.

Welding path	Welding layer	Welding current (A)	Welding voltage (V)	Welding speed (mm/min)	Shielding gas flow rate (L/min)
1	Backing welding	115–125	19.6–20.5	240–280	18–20
2	Covering welding	120–130	20.2–21.1	240–280	18–20
3	Covering welding	125–130	20.5–21.1	250–300	18–20

Table 1. Welding experiment parameters.

Fig. 10. Welding test specimens of ECPs.

with a baffle featuring a hydraulic pump interface, while the other end was welded with a sealing baffle. At this point, the ECP measured 224 mm in maximum diameter and 177 mm in minimum diameter, as shown in Fig. 11. The ECP was then pressurized by a hydraulic pump to 26 MPa, at which point it fully expanded. During the pressurization process, the welded seam exhibited good ductility and remained crack-free. The final ECP exhibited a maximum diameter of 267 mm and a minimum diameter of 264 mm, as depicted in Fig. 12. The welded seam, as shown in Fig. 13, remained crack-free throughout the deformation of the ECP, indicating that the weld quality meets the required standards. This demonstration underscores the capability of the ECP mobile welding robot to reliably perform automatic butt-welding operations on ECPs.

In summary, the flexible contour tracing mobile welding robot for ECP proposed in this paper can efficiently complete the butt-welding task for 8-shaped ECPs. This robot frees humans from laborious and complex welding tasks, solves the industrial challenge of achieving automated welding on complex curved welds in limited spaces, and improves welding efficiency while ensuring satisfactory weld quality. Furthermore, this design concept can be extended to other complex welding scenarios in the manufacturing industry, compensating for the limitations of conventional welding robots in specific applications. It promotes high-quality development in manufacturing and provides reliable technical solutions for the upgrading of intelligent manufacturing industries.

Conclusion

Addressing the industrial challenge of achieving automatic welding for complex-shaped ECPs in confined spaces and with irregular cross-sections, a flexible contour tracing mobile welding robot specifically designed for welding on complex curved seams has been developed. A dynamic analysis and calculation of the robot's drive system was conducted, revealing that creating a smaller angle between force and velocity can effectively reduce the loss of driving force transmission. A transmission model was established, and finite element analysis was performed on the critical areas of the contour tracing track. Furthermore, a life prediction of the ECP mobile welding robot was conducted based on the Archard model, which indicates that the system can operate stably for a long time. A virtual simulation test platform was set up to simulate the robot's motion trajectory, verifying

Fig. 11. ECP specimen before pressurization.

Fig. 12. ECP specimen pressurized to 26 MPa.

the rationality of the mechanical structure design. A prototype was developed, and welding and inflation tests were conducted to verify the reliability of the robot's welding seams, thus solving the industrial challenge of achieving automated welding in confined spaces and on complex curved seams. However, the welding torch actuator designed in this paper, which is located at the end of the mobile welding robot, has not yet achieved real-time automatic adjustment. Future work will focus on further optimizing the relevant structures to enhance the robot's intelligent operation level.

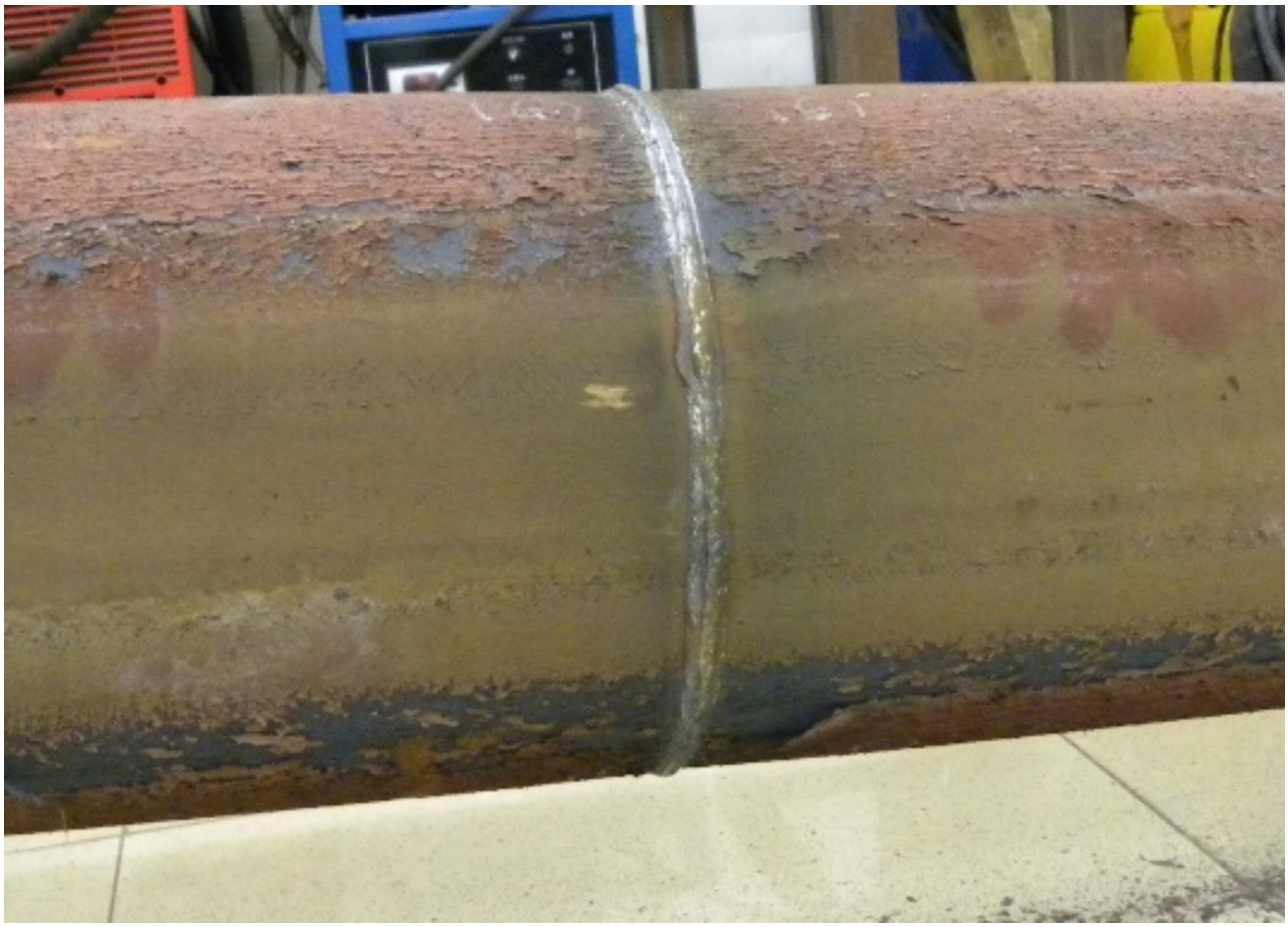

Fig. 13. Fully expanded state of welding seam on ECP.

Data availability

All data is provided within the manuscript.

Received: 22 July 2024; Accepted: 3 March 2025
Published online: 10 March 2025

References

1. Shi, L., Tian, X. C. & Zhang, C. H. Automatic programming for industrial robot to weld intersecting pipes. *Int. J. Adv. Manuf. Tech.* **81**, 2099–2107. https://doi.org/10.1007/s00170-015-7331-8 (2015).
2. Fang, L. J. & Sun, L. F. Design of a novel robotic arm with non-backlash driving for friction stir welding process. *Int. J. Adv. Manuf. Tech.* **93**, 1637–1650. https://doi.org/10.1007/s00170-017-0617-2 (2017).
3. Guo, W. J., Zhu, Y. G. & He, X. A robotic grinding motion planning methodology for a novel automatic seam bead grinding robot manipulator. *IEEE Access.* **8**, 75288–75302. https://doi.org/10.1109/ACCESS.2020.2987807 (2020).
4. Bozek, P. Robot path optimization for spot welding applications in automotive industry. *Teh Vjesn.* **20**, 913–917 (2013).
5. Fang, H. C., Ong, S. K. & Nee, A. Y. C. Robot path planning optimization for welding complex joints. *Int. J. Adv. Manuf.* **90**, 3829–3839. https://doi.org/10.1007/s00170-016-9684-z (2017).
6. Geng, Y. S., Zhang, Y. K., Tian, X. C. & Zhou, L. L. A novel 3D vision-based robotic welding path extraction method for complex intersection curves. *Robot Cim-int Manuf.* **87**, 102702. https://doi.org/10.1016/j.rcim.2023.102702 (2024).
7. Wang, J. et al. Intelligent wheeled mobile robot for spherical tank welding. In *Proc. SPIE* 4573 (pp. 244–255), SPIE, (2002). https://doi.org/10.1117/12.457449
8. Liang, Y. et al. Research on flexible R ail type all-position welding robot. *Electr. Weld. Mach.* **38**, 23–26 (2008). (In Chinese).
9. Guo, J., Zhu, Z., Sun, B. & Zhang, T. A novel field box girder welding robot and realization of all-position welding process based on visual servoing. *J. Manuf. Process.* **63**, 70–79. https://doi.org/10.1016/j.jmapro.2020.04.054 (2021).
10. Gonzalez-De-Santos, P., Armada, M. A. & Jimenez, M. A. An industrial walking machine for naval construction. In Proceedings of the 1997 IEEE International Conference on Robotics and Automation. *IEEE*, pp. 28–33 (1997).
11. Santos, P. G., d., Armada, M. A. & Jimenez, M. A. Ship Building with ROWER. *IEEE Robot Autom. Mag.* **7**, 35–43. https://doi.org/10.1109/100.894031 (2000).
12. Lee, D. et al. Development and application of an intelligent welding robot system for shipbuilding. *Robot Cim-int Manuf.* **27**, 377–388. https://doi.org/10.1016/j.rcim.2010.08.006 (2011).
13. Oh, M., Lee, S. M., Kim, T., Lee, K. Y. & Kim, J. Design of a teaching pendant program for a mobile shipbuilding welding robot using a PDA. *Comput. Aided Des.* **42**, 173–182. https://doi.org/10.1016/j.cad.2009.09.005 (2010).
14. Lee, D. et al. Development of a mobile robotic system for working in the double-hulled structure of a ship. *Robot Cim-int Manuf.* **26**, 13–23. https://doi.org/10.1016/j.rcim.2009.01.003 (2010).

15. Ku, N., Ha, S. & Roh, M. I. Design of controller for mobile robot in welding process of shipbuilding engineering. *J. Comput. Des. Eng.* **1**, 243–255. https://doi.org/10.7315/JCDE.2014.024 (2014).
16. Ku, N., Lee, D., Lee, K. Y. & Kim, J. Development of a mobile welding robot for double-hull structures in shipbuilding. *J. Mar. Sci. Tech.* **15**, 374–385. https://doi.org/10.1007/s00773-010-0099-5 (2010).
17. Lee, D., Seo, T. & Kim, J. Optimal design and workspace analysis of a mobile welding robot with a 3P3R serial manipulator. *Robot Auton. Syst.* **59**, 813–826. https://doi.org/10.1016/j.robot.2011.06.004 (2011).
18. Kermorgant, O. A magnetic climbing robot to perform autonomous welding in the shipbuilding industry. *Robot Cim-int Manuf.* **53**, 178–186. https://doi.org/10.1016/j.rcim.2018.04.008 (2018).
19. Goh, C. F. et al. Designing a mobility solution for fully autonomous welding of double-hull blocks. *J. Mech. Robot.* **11**, 045002. https://doi.org/10.1115/1.4043604 (2019).
20. Goh, C. F., Vazquez-Santiago, K. & Shimada, K. Landing a mobile robot safely from tall walls using manipulator motion generated from reinforcement learning. In *16th IEEE International Conference on Automation Science and Engineering (CASE)*, *IEEE*, pp. 8–15, (2020). https://doi.org/10.1109/CASE48305.2020.9216977 (2020).
21. Chen, X., Dharmawan, A. G., Foong, S. & Soh, G. S. Seam tracking of large pipe structures for an agile robotic welding system mounted on scaffold structures. *Robot Cim-int Manuf.* **50**, 242–255. https://doi.org/10.1016/j.rcim.2017.09.018 (2018).
22. O'Toole, A. T. & Canfield, S. L. Developing a kinematic estimation model for a climbing mobile robotic welding system. In *International Design Engineering Technical Conferences and Computers and Information in Engineering Conference*, *ASME*, pp. 1187–1194, (2010). https://doi.org/10.1115/DETC2010-28878
23. Stacy, J., Langley, D. & Canfield, S. L. Process qualification for a mobile robotic welding system through manipulability. In *International Design Engineering Technical Conferences and Computers and Information in Engineering Conference*, *ASME*, pp. 941–950, (2012). https://doi.org/10.1115/DETC2012-71382
24. Gawande, S. H. A combined numerical and experimental study on metal expansion bellows for STHE. *J. Braz Soc. Mech. Sci.* **40**, 465. https://doi.org/10.1007/s40430-018-1382-3 (2018).
25. Jeon, B. G., Kim, S. W., Yun, D. W., Ju, B. S. & Son, H. Y. An experimental study on seismic performance evaluation of multi-ply bellows type expansion joint for piping systems. *Sustainability* **14**, 14777. https://doi.org/10.3390/su142214777 (2022).
26. Li, M. et al. A new method for intelligent prediction of drilling overflow and leakage based on multi-parameter fusion. *Energies* **15**, 5988. https://doi.org/10.3390/en15165988 (2022).
27. Chen, Y. L., Liu, J. & Cai, M. Q. Three-dimensional nonlinear coupling vibration of drill string in deepwater riserless drilling and its influence on wellbore pressure field. *Nonlinear Dynam.* **111**, 14639–14666. https://doi.org/10.1007/s11071-023-08625-1 (2023).
28. Li, Q. C. et al. Experimental investigation on hydrate dissociation in near-wellbore region caused by invasion of drilling fluid: ultrasonic measurement and analysis. *Environ. Sci. Pollut R.* **29**, 36920–36937. https://doi.org/10.1007/s11356-021-18309-1 (2022).
29. Tao, X., Zhu, H., Zeng, Y. & Xu, L. Development and mechanism motion analysis of welding robot for expandable profile liner. *J. China Univ. Petroleum.* **35**, 119–128 (2011). (In Chinese).
30. Fang, J. L. et al. A shift from efficiency to adaptability: Recent progress in biomimetic interactive soft robotics in wet environments. *Adv. Sci.* **9**, 2104347. https://doi.org/10.1002/advs.202104347 (2022).
31. Wang, C. J. et al. Soft ultrathin electronics innervated adaptive fully soft robots. *Adv. Mater.* **30**, 1706695. https://doi.org/10.1002/adma.201706695 (2018).
32. Cheng, Y. B., Chen, L. X., Ge, P. Y., Chen, X. M. & Niu, J. X. Design and optimization of dual-phase chain transmission system based on single tooth chain plate. *Mech. Based Des. Struc.* **51**, 899–913. https://doi.org/10.1080/15397734.2020.1856683 (2023).
33. Zhang, S. P. & Tak, T. O. Efficiency Estimation of roller chain power transmission system. *Appl. Sci.* **10**, 7729. https://doi.org/10.3390/app10217729 (2020).
34. Yang, Z., Hou, J., Liu, Q. L. & Cho, C. D. Stress and strain concentrations for the filleted shafts in tension. *Adv. Sci. Lett.* **4**, 2631–2636. https://doi.org/10.1166/asl.2011.1729 (2011).
35. Zhou, Y. C., Lin, Q. Y., Hong, J. & Yang, N. Optimal design of functionally graded material for stress concentration reduction. *Structures* **29**, 561–569. https://doi.org/10.1016/j.istruc.2020.11.053 (2021).
36. Hu, J. Q., Song, H. X., Sandfeld, S., Liu, X. M. & Wei, Y. G. Breakdown of Archard law due to transition of wear mechanism from plasticity to fracture. *Tribol Int.* **173**, 107660. https://doi.org/10.1016/j.triboint.2022.107660 (2022).
37. Huang, T. C., Lin, C. Y. & Liao, K. C. Sealing performance assessments of PTFE rotary lip seals based on the elasto-hydrodynamic analysis with the modified Archard wear model. *Tribol Int.* **176**, 107917. https://doi.org/10.1016/j.triboint.2022.107917 (2022).
38. Aghababaei, R. & Zhao, K. Micromechanics of material detachment during adhesive wear: A numerical assessment of Archard's wear model. *Wear* **476**, 203739. https://doi.org/10.1016/j.wear.2021.203739 (2021).

Acknowledgements

This research was supported by the National Key Research and Development Program of China (No. 2023YFB3407700).

Author contributions

All authors participated in the conception of the article and contributed to the manuscript. S.Y., L.X., and J.H. were responsible for organizing and collecting the materials for the paper. S.Y. led the research and writing of this article, while L.X. provided financial support for the research, and J.H. offered guidance on the overall research approach. B.C., R.Z., and F.H. completed the translation and organization of relevant literature, translated and polished the first draft of the paper, and assisted in conducting the experiments. Ultimately, all authors reviewed and approved the final manuscript.

Declarations

Competing interests

The authors declare no competing interests.

Additional information

Correspondence and requests for materials should be addressed to L.X. or J.H.